Volume 1 | Number 1 | Jan 2013 | Pages 1–100

Journal of
Materials Chemistry A

Materials for energy and sustainability
www.rsc.org/materialsA

ROYAL SOCIETY
OF CHEMISTRY

ROYAL SOCIETY
OF CHEMISTRY

www.rsc.org/materialsA

Journal Name

RS

ARTICLE

Sculpturing Metal Foams toward Bifunctional 3D Copper Oxide Nanowire Arrays for Pseudo-capacitance and Enzyme-free Hydrogen Peroxide Detection†

Jianfei Huang, Huailong Li, Yihua Zhu*, Qilin Cheng, Xiaoling Yang and Chunzhong Li*

Commercial copper foams have been tailored by a highly scalable method combining room-temperature wet-chemical etching and hydroxide thermolysis into three-dimensional copper oxide nanowire arrays/copper (3D-CuONA/Cu) composite with macroporous voids and large-area fur-like nanowire array structures, whose structures and compositions were studied employing electron microscopy, X-ray diffraction (XRD) and Raman spectroscopy. The 3D-CuONA/Cu composite monolith was applied as free-standing electrodes for pseudo-capacitive energy storage and enzyme-free H_2O_2 detection. Thanks to the 3D electrode architecture and high-density *in situ* formed electroactive nanoarrays, an enhanced capacitance of 608 mF cm^{-2} at 2 mV s^{-1} was achieved, with 88.6% capacity retention after 4000 cycles observed at a high current density of 30 mA cm^{-2}. For enzyme-free H_2O_2 sensing, an extraordinary sensitivity of 5.75 mA mM^{-1} cm^{-2} and a low detection limit of 0.56 uM were achieved. The prototype sensor also exhibited eligible selectivity and feasibility for real sample analysis.

Introduction

The increasingly high demands for renewable energy, clean power sources, environmental protection and life comfortability have posed great challenges for building highly efficient electrochemical systems including rechargeable batteries, supercapacitors, fuel cells, water-splitting (photo)electrolysers, electro-fenton devices, and chemosensors.[1-5] Electrode materials are core entities that exert dominating influences on the performance for these cases. On the scope of promoting electrode kinetics *via* nanostructured electrode materials, simultaneous design and preparation of free-standing (self-supported, binder-free, monolithic, etc.) active material-loaded electrodes are being emphasized and are gaining preference compared to powdery immobilization approaches. Importantly, such an *in situ* synthetic scheme elegantly circumvent those notorious drawbacks such as time-consuming and tedious manual operations, electro-inactivity and poor conductivity of binders, high mass transport resistance, unwanted blocking of active materials, and moderate mechanical adhesion between active materials and current collectors, therefore being able to access enhanced electrochemical performance with their highly integrated style, mechanical robustness and efficient charge/mass transport.[6-9] Among diverse monolithic electrode

architectures, 3D nanostructured electrodes based on commercially available metal foams with complex geometries have been investigated for a wide variety of applications, because they can achieve more sufficient electrolyte/electrode interfacing by providing macroporous and interconnected voids for electrolyte penetration while guarantee good current collection with the integral conducting scaffold.[10] Consider potential industrial-scale production, a prerequisite lies in low cost and scalability of the preparation techniques. Unfortunately, most protocols toward 3D nanostructured foams rely heavily on hydrothermal methods,[11] vapour deposition,[12] high-temperature annealing,[13] and electrodeposition,[14] which are plagued by harsh conditions (high temperature and pressure), complicated equipment set-ups, difficult scaling-up of hardware dimensions and/or requirement for high-quality raw materials. In this regard, room-temperature solution- processed routes under mild conditions are highly attractive as an alternative for manufacturing monolithic electrochemical electrodes with delicate microstructures in large batches.

Copper (II) oxide (CuO), a typical p-type semiconducting material that has received extensive exploration due to its multi-functionality and relative abundance in nature, has shown versatile capabilities in a number of applications varying from

photocatalysis, chemical sensing, photodetector to rechargeable batteries and solar-to-fuel cells.[15-19] Specifically, electroactive CuO can be applied for electrochemical energy storage with its pseudo-capacitive properties. Rather than storing energy *via* electric double layer capacitance (EDLC) like carbon-based supercapacitors, pseudo-capacitance has the energy stored through reversible redox reactions occurring at the surface of electro-active materials and generally offers higher capacity than the EDLC-based capacitors.[20] Previously, CuO-based supercapacitors processed by powdery techniques have been intensively investigated. For example, Yan et al reported porous CuO nanobelts/single-walled carbon nanotubes flexible electrodes that delivered high energy density of 130.2 W h kg^{-1} in LiPF$_6$/EC:DEC.[21] Zhang et al investigated dependence of pseudo-capacitance on the morphologies of diverse CuO nanostructures.[22,23] Direct grown nanostructured CuO on current collectors also gained attentions, having been realized *via* electrochemical anodization and electro-oxidation,[24] successive ion layer adsorption reaction,[25] electrodeposition,[26] hydrothermal method,[27] and chemical bath deposition.[28] In addition to electrochemical energy storage, copper oxide have also seen tremendous work on electrochemical sensing of hydrogen peroxide, glucose, hydrazine and dopamine,[29-32] which mainly utilized the electrocatalytic capability of copper oxide in either binder-free or binder-cocasted forms. Yet for all that, it is still challenging to bring cost-effectiveness to nanostructured CuO-based free-standing electrodes using scalable methods for versatile application occasions.

Driven by the above motivations, we herein present the combination of wet-chemical treatment and low-temperature thermolysis to synthesize 3D CuO nanowire arrays/Cu (3D-CuONA/Cu) composite. The former step, related to the formation of nanowire arrays, is based on alkaline oxidation of metallic copper substrate, similar to anodization of copper in alkaline media.[33,34] Differently, a facile immersion method is employed to exempt the complexity and maintenance of the electrochemical device set-ups. Integrated as free-standing electrodes, the composite foam showed promising performance for pseudo-capacitive energy storage and enzyme-free sensing of H$_2$O$_2$. At a scan rate of 2 mV s^{-1}, an areal capacitance of 608 mF cm^{-2} was achieved, along with an 88.6% capacity retention after 4000 cycles at a high current density of 30 mA cm^{-2}. For electrochemical detection of H$_2$O$_2$, the sensor electrode based on the 3D-CuONA/Cu composite exhibited a remarkably high sensitivity of 5.57 mA mM^{-1}cm^{-2} and a detection limit reaching sub-micromolarity, and primitively showed its potential for determining H$_2$O$_2$ in real milk samples.

Results and discussions

Unlike most bottom-up synthetic methods where precursor species were *ex situ* introduced to form the desired nanostructures on the 3D substrate in an "add-on" manner, the present work employs the 3D substrate directly as the precursor and tailors its surface into nanowire arrays *via* a top-down strategy. The route and method are schematically illustrated in Fig. 1a, which can be accomplished by mainly two steps,

namely immersing the starting materials in a reactant solution at room temperature and placing it on a hot plate for a period of time. This method is very facile, economical and efficient, which holds great potential for mass production. Successful realization of the this strategy was clearly perceivable by the colour evolution of the samples from shining orange to light blue, and eventually to dark brown, as also shown in the digital photograph in Fig. 1a.

The microstructures of the 3D-CuONA/Cu composite and the intermediates were studied by scanning electron microscopy (SEM) shown in Fig. 1. As shown in Fig. 1c1, large-area CuO nanowire arrays can be found to densely and uniformly cover the surface of the macroporous scaffold of Cu foam and they feature grass-like arrays structure in long-range microscale. This hierarchical configuration combining *in situ* formed 1D high-density electroactive material nanoarrays and 3D porous scaffold is favorable for facilitated electrolyte penetration by providing large surface areas and mass diffusion pathways.[18,35] At higher magnifications, it is found that the nanowire length is about 10 um with the diameters varying from 100 to 250 nm. Compared to the Cu(OH)$_2$ nanowire arrays (Cu(OH)$_2$NA) intermediate shown in Fig. 1b, morphological variance after thermolysis is negligible, which may be thanks to the relatively low annealing temperature that prevented destruction or deformation of the 1D wire morphology and 3D arrays structure.[36,37] Formation of the arrays of 1D Cu(OH)$_2$ precursor is possibly associated with olation reaction that has been discussed elsewhere.[38] Specifically, the copper$^{(0)}$ is oxidized by the oxidant and dissolves in the solution as Cu^{2+}, which interacts with OH$^-$ ligands to form distorted Cu(OH)$_6$ octahedral. By stacking the sheets that are formed by the Cu(OH)$_6$ sharing edges along the [100] direction because of the relatively strong hydrogen bond linkages, the 1D morphology is obtained.[39] The final morphology of the obtained structure is time-dependent. As shown in Fig. S1, the nanowire length increased at the beginning of the reaction, suggesting a basal growth manner. The growth speed then slowed down after a certain duration and the nanowire length stabilized at around 11-12 um after 30 min-immersion. Upon further prolonging the duration, flower-like structure were found to form on the nanowire arrays (Fig. S1d).

Transmission electron microscopy (TEM) characterization was conducted to gain more structural information. As shown in Fig. 2a, a single CuO nanowire was photographed. The observed nanowire features a tapering manner from the 'root' to the 'tip', and is about 130-240 nm in diameter, in consistence with the SEM analysis. Notably, the length of the nanowire in the TEM is generally shorter than that estimated from the SEM characterization. This may be resulted from the mechanical breakage of the nanowires during the preparation of the TEM samples. A magnified TEM image for CuO nanowire is shown in Fig. 2b. This is common for metal oxide nanowire prepared from thermolysis of their precursors, where volatile substances such as H$_2$O diffuse away with voids left in the solid bulk. To soundly conclude the composition of the samples, X-ray diffraction (XRD) and Raman spectroscopy were conducted,

and the patterns are shown in Fig. 2c and 2d, respectively. For the XRD, pattern (b) presents typical signals from the Cu foam

after wet-chemical treatment, whose diffraction peaks at 16.9°, 23.9°, 34.1°, 36.0°, 38.2°, 39.9° and 53.4° can be respectively
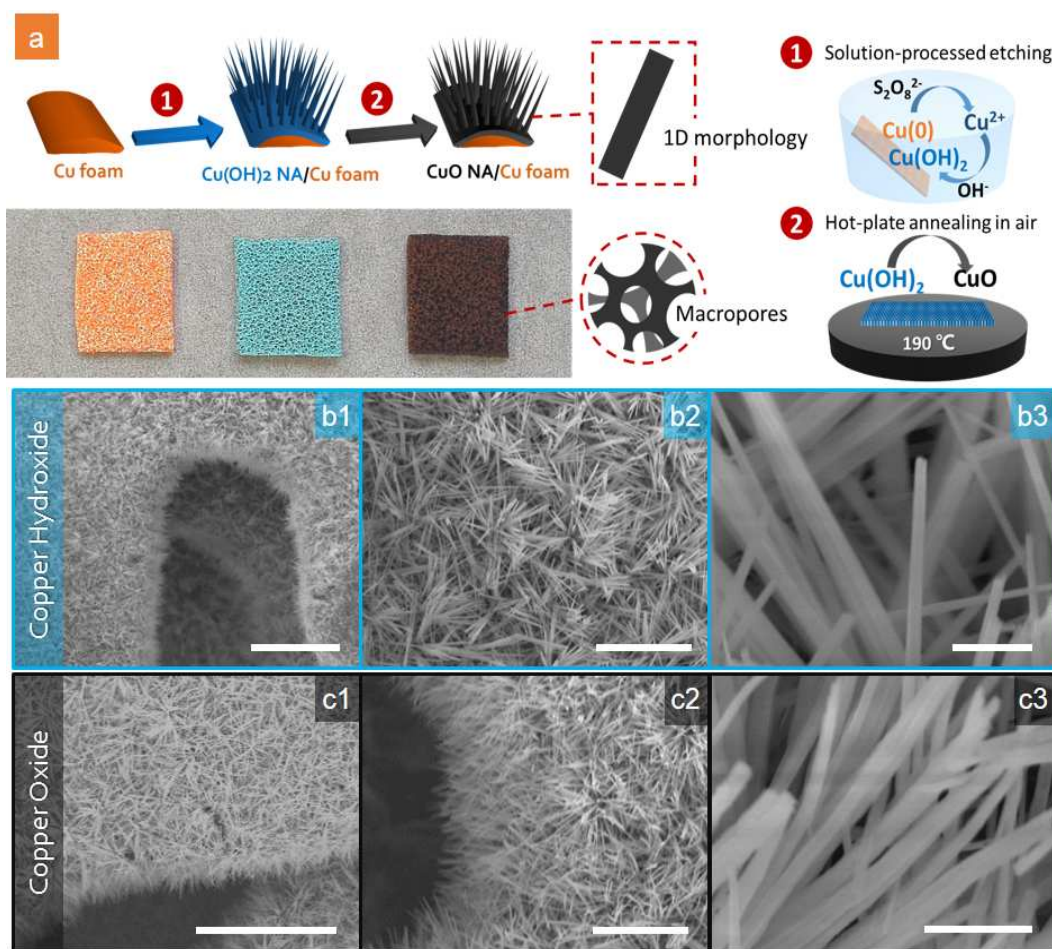
Fig. 1 (a) Synthetic route, preparation method, and samples' digital photographs. SEM images of Cu(OH)$_2$NA/Cu (b) and 3D-CuONA/Cu (c) composite foams at different magnifications. Scale bars from left to right in (b) and (c) are 50, 15 and 1 um, respectively.

indexed to the (020), (021), (002), (111), (022), (130) and (150) planes of the orthorhombic structured Cu(OH)$_2$. The signals from the metallic copper at 43.5°, 50.6° and 74.3° are also clearly recognizable and are ascribed to the 3D Cu scaffold. Pattern (a) is for the 3D-CuONA/Cu composite, from which the disappearance of diffractions peaks of Cu(OH)$_2$ and presence of characteristic diffraction peaks for monoclinic CuO around 35.6° and 38.5° suggest the successful transformation from Cu(OH)$_2$ to CuO. The moderate signal intensity from CuO may be due to the fact that the grains of CuO are rather small, and the stronger signals from the substrate of metallic copper, whose diffraction signals still exist and are quite obvious, evidencing limited oxidation of the Cu substrate under the relative low heating temperature (190 °C) and coverage of the dense nanowire arrays structures, which guarantees good conductivity of the current collector. Formation of CuO is also corroborated by employing Raman spectroscopy, and a typical spectra is shown in Fig. 2d. The peaks situated around 291, 339 and 621 cm^{-1} correspond to Ag, B$_g^1$ and B$_g^2$ modes of bulk CuO, respectively. These results proved the feasibility of the

preparation scheme toward the high-density 1D CuO nanostructures on 3D conductive metal foam.

The merit of the monolithic 3D-CuONA/Cu composite was first evaluated as electrodes for electrochemical energy storage. As was mentioned, the *in situ* preparation style essentially exempts the necessity of employment of binders or conductive additives, which, though undesirable considering the tedious manipulations and increased costs, as well as possibility of blocking active materials, are indispensable for powder-based electrode fabrication methodologies. Further, *in situ* nanoengineering of 3D monolithic electrode favours high loading of active materials compared to slurry-pasting protocols, and thus giving rise to a higher areal specific capacitance. Herein, the 3D-CuONA/Cu composite was directly fashioned into a free-standing electrode, thus making the post-assembly of devices further simplified. Fig. 3a presents the cyclic voltammetry (CV) profile of the 3D-CuONA/Cu at 2 mV s^{-1} in 1M NaOH. The CV curve is quite different from a typical quasi-rectangular one for carbonaceous supercapacitors that store energy under EDLC mechanism. Moreover, the

reduction peaks obviously shift in cathodic direction and the current density enlarges as the scan rate increases from 2 to 100 mV s^{-1}, as shown in Fig. 3b. These CV behaviours indicate
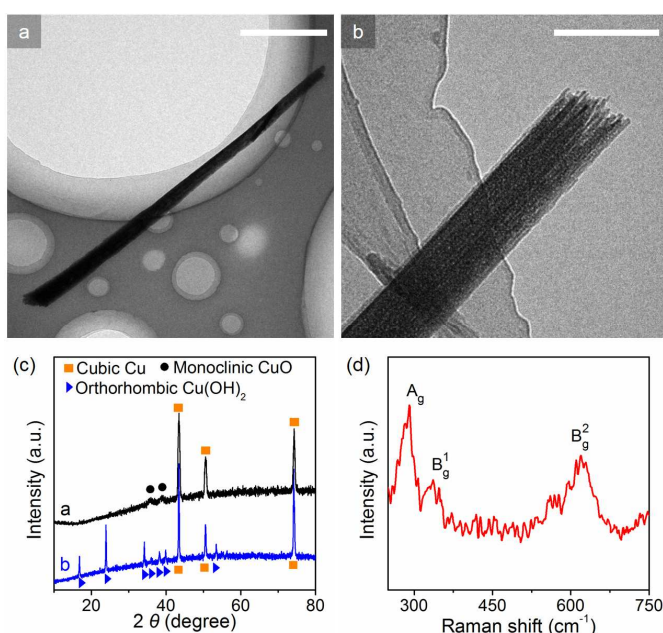
Fig. 2 TEM image of a single CuO nanowire at low (a) and high (b) magnifications. Scale bars are 1 um and 200 nm for (a) and (b), respectively. (c) XRD patterns of 3D-CuONA/Cu and its Cu(OH)$_2$NA/Cu precursor. (d) Raman spectra of the 3D-CuONA/Cu.

can be viewed from Fig. 3a, the anodic and cathodic peaks in the potential range are quite broad. The unobvious and slightly humping feature of the peaks is possibly caused by complexity of redox reactions of copper oxide species in alkaline solution, which might further overlapping each other, and high resistivity from species like Cu(OH)$_2$ can also be a reason. Despite the complexity of electrochemical reaction of copper oxide-based materials under alkaline media, the pseudo-capacitance can be generally attributed to the following reactions:[25]

$$Cu_2O + 2OH^- \leftrightarrow 2CuO + H_2O + 2e^-$$

$$Cu_2O + H_2O + 2OH^- \leftrightarrow 2Cu(OH)_2 + 2e^-$$

$$CuOH + OH^- \leftrightarrow CuO + H_2O + e^-$$

$$CuOH + OH^- \leftrightarrow Cu(OH)_2 + e^-$$
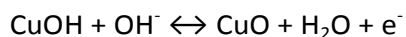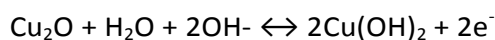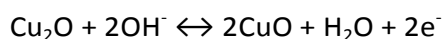
To illustrate the enhancement from the dense CuO nanowire arrays, CV curve is also plotted in Fig. 3a for thermally oxidized copper oxide/copper (TO-CuO/Cu) foam prepared by direct dry oxidation at 300 °C in air, which was supposed to provide mainly planar CuO (see more data in the Electronic Supplementary Information, ESI) covering the surface of the macroscopic foam. Even with some scattered CuO nanowires on its surface as a plus (Fig. S2b), the TO-CuO/Cu still showed much smaller magnitude of current density, implying a much smaller capacitance. Galvanostatic discharge curves in Fig. 3d

pseudo-capacitive features for the 3D-CuONA/Cu composite.[24] Also   as

demonstrate similar results by showing a considerably prolonged discharge time for the 3D-CuONA/Cu than the TO-CuO/Cu. Such differences suggest the importance of the high-density CuO nanowire arrays that provide significantly increased electrochemically active sites for the redox interactions and energy storage. Nanoengineering of the copper foam endows the substrate with dense nanowire arrays structure, leading to much higher specific surface area (surface area per geometric area) compared to the planar surface-dominated TO-CuO/Cu, and hence higher capacitance. Fig. 3e presents the discharge curves of the 3D-CuONA/Cu at different current densities. It is found the IR drop is relatively large. We speculate it an outcome of high resistivity inherent to copper oxides and worsened by packing of dense nanostructure layer, whose solution requires further tuning synthesis parameters and/or incorporating other highly conductive materials such as carbon, graphene, metal nanoparticles and conductive polymers. CV and galvanostatic tests for the TO-CuO/Cu at various scan rates and current densities are shown in Fig. S3. It is found that at all the scan rates (2-100 mV s^{-1}) and current densities (5-30 mA cm^{-2}) investigated here, the 3D-CuONA/Cu exhibited larger capacitance than the TO-CuO/Cu by one order of magnitude, as displayed in Fig. 3c and 3f. An areal specific capacitance of 608 mF cm^{-2} was achieved by the 3D-CuONA/Cu at 2 mV s^{-1}, which was 535 mF cm^{-2} under galvanostatic mode at 5 mA cm^{-2}, showing 7-fold and 19-fold improvement compared to the TO-CuO/Cu under the respective testing configurations. Capacity parameters under different testing conditions are detailed in Tab. S1. The 3D-CuONA/Cu marks a significant enhancement over a series of copper compound-engaged supercapacitor electrodes including ZnO@CuS@PEDOT@MnO$_2$ core-shell nanorod arrays (19.85 mF cm^{-2} at 5 mV s^{-1}),[40] electrodeposited porous and amorphous copper oxide film (25.1 mF cm^{-2} at 20 mV s^{-1}),[41] Cu(OH)$_2$ thin films (34 mF cm^{-2} at 10 mV s^{-1}),[42] CuS nanowire arrays (91.5 mF cm^{-2} at 0.6 mA cm^{-2}),[43] lotus-like CuO/Cu(OH)$_2$ hybrid (97.3 mF cm^{-2} at 2 mA cm^{-2}),[44] vertical CuO nanoflakes (175 mF cm^{-2} at 2 mA cm^{-2}),[45] CuO nanoribbon-on-Ni-nanoporous/Ni foam (281.6 mF cm^{-2} at 10 mV s^{-1}),[26] and MnO$_2$-coated CuO flower-like nanostructures (334.4 mF cm^{-2} at 0.6 mA cm^{-2}),[46] and is superior to other pseudo-capacitive electrodes such as Fe$_3$O$_4$/SnO$_2$ core-shell nanorod (7.013 mF cm^{-2} at 0.20 mA cm^{-2}),[47] Ni/NiO core-shell inverse opals (~9 mF cm^{-2} at 5 mV s^{-1})[48] and porous Co$_3$O$_4$ nanowall (~520 mF cm^{-2} at 3.2 mA cm^{-2}).[49] When consider weight-normalized capacitance, the capacitance is not ideal (170 F g^{-1}). It could be attributed to the packing of active materials which results in "dead materials" that serve insufficiently for the purpose of pseudo-capacitance, accompanied with the relatively high loading mass (3.58 mg cm^{-2}). In spite of this, improving the parameter by reducing loading mass is not a meaningful approach because it possibly means high electrode area or volume, and for some occasions demanding downsized devices,

this is unfavorable. Hence, there is still necessity in future work to seek a balance between loading mass and weight-normalized capacitance. Notably, hybridizing with other electroactive materials with higher theoretical capacity to further improve the capacity performance is presumably compatible to the present synthetic scheme and is being investigated.
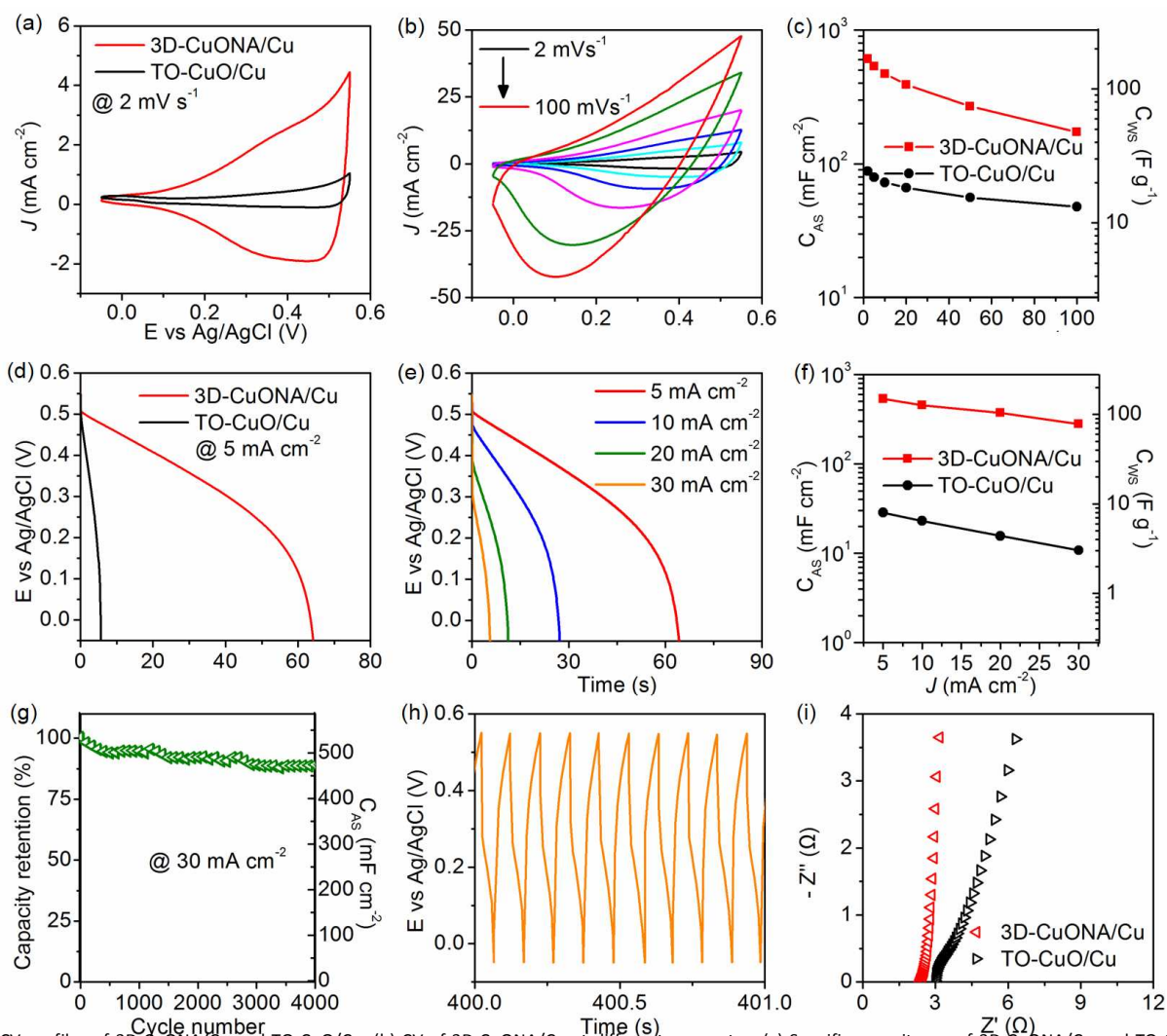
Fig. 3 (a) CV profiles of 3D-CuONA/Cu and TO-CuO/Cu. (b) CV of 3D-CuONA/Cu at different scan rates. (c) Specific capacitance of 3D-CuONA/Cu and TO-CuO/Cu at different scan rates. (d) Galvanostatic discharge curves of 3D-CuONA/Cu and TO-CuO/Cu. (e) Galvanostatic discharge curves of 3D-CuONA/Cu at different current densities. (f) Specific capacitance of 3D-CuONA/Cu and TO-CuO/Cu at different current densities. (g) Comparison of CV curves of 3D-CuONA/Cu before and after 5000 cycles at 100 mV s^{-1}. (h) Cycling performance of 3D-CuONA/Cu measured by galvanostatic tests. Inset shows charge-discharge cycling over 40000 s. (i) Zoom-in Nyquist plots of 3D-CuONA/Cu and TO-CuO/Cu.

The cycling stability is an essential requirement for energy storage devices. Considering the relatively higher power density of supercapacitors in practical usage, it is rational to test the cyclability at high power output.[50] Therefore, the cycling performance was evaluated at a high current density of 30 mA cm^{-2} under successive repeated galvanostatic charge-discharge test, and the result for 4000 cycles is displayed in Fig. 3g. The capacity retention at the end of 2000 cycles is 91.8%, comparable to the electrospun copper oxide nanowire electrode (92% at 12.5 mA cm^{-2}).[51] After further prolonging cycle number to 4000, the capacity retention stabilized around 88.6%. In Fig. 3h, the successive charge-discharge curve is presented that demonstrates stable cycling behaviour at a long runtime over 40,000 s. This long-run cyclability outperforms the copper

oxide nanoparticles on graphene oxie nanosheets (79% after 1000 cycles at 0.25 A g^{-1}),[52] CuO/SWCNT networks (58.0% after 1000 cycles at 5 A g^{-1}),[53] CuO nanosheet arrays on Ni foam (82.5% after 500 cycles at 5 mA cm^{-2}),[27] and CuO cauliflowers (81% after 2000 cycles at 100 mV s^{-1}).[54] From the SEM image of 3D-CuONA/Cu after the cycling tests (Fig. S4), we can see that the overall morphology of the 3D-CuONA/Cu remained as nearly the same as the freshly prepared samples, which is consistent to the good cycling stability. Thus, the excellent stability is believed to be benefited from the robust mechanical adhesion intrinsic to *in situ* synthesis and 3D structure of the nanowire arrays, which suppressed destruction of crystalline and morphological structures of the active materials during the ion insertion and extraction.

Electrochemical impedance spectroscopy was conducted and the corresponding Nyquist plots are presented in Fig. 3i. As presented, the equivalent series resistance (ESR) of the 3D-CuONA/Cu (2.4 Ω) is smaller than the TO-CuO/Cu (3.0 Ω), which implies facilitated charge transfer kinetics with the 3D-CuO nanowire arrays compared with the planar CuO surface
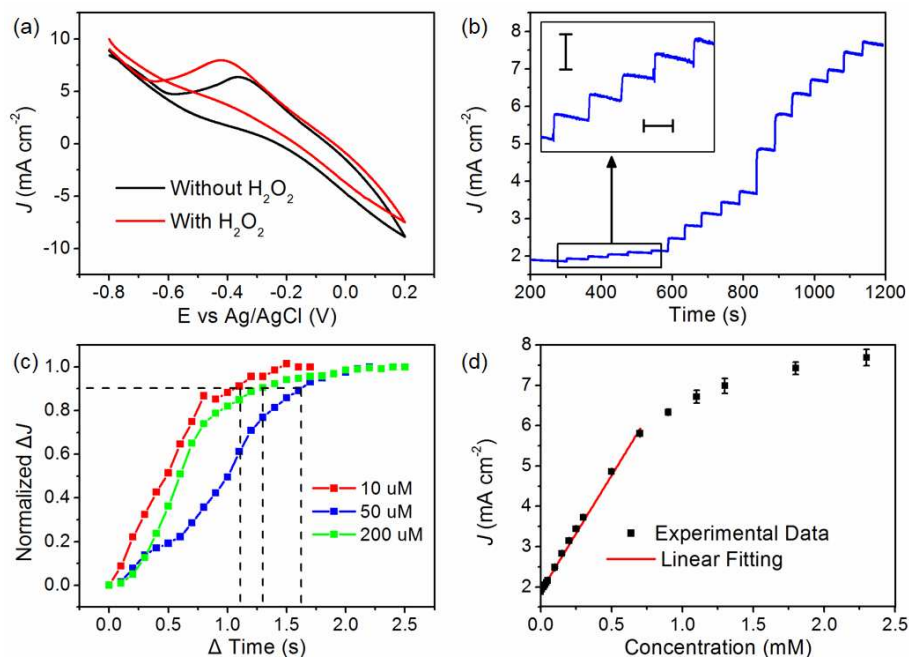
Fig. 4 (a) CV curves of 3D-CuONA/Cu with and without 4 mM H_2O_2 at a scan rate of 50 mV/s. (b) J-t curve of 3D-CuONA/Cu under -0.4 V. Inset: current responses at low concentration levels. Scale bars are 100 uA cm^{-2} (vertical) and 50 s (horizontal). Analyte introduction is 5-time addition of 10, 50, 200 uM and 500 uM for each and 2-time addition of 500 uM. (c) Normalized ΔJ-Δt curve of response time. (d) Calibration plot for 3D-CuONA/Cu.

formed by thermal oxidation. In addition, since the straight line in the Warburg diffusion region corresponding to the low-frequency part of the Nyquist plot shows obviously larger slope for the 3D-CuONA/Cu, a lower mass transfer resistance is suggested in the case of the 3D-CuONA/Cu, which may be ascribed to short ion diffusion distance associated with the 1D morphology and the arrayed nanostructures.[45] Therefore, it can be inferred that the 3D-CuONA/Cu composite foam may also be a suitable tool for other electrochemical applications such as electroanalysis.

Hydrogen peroxide (H_2O_2) is a chemical of considerable interests in biological research scopes as well as industrial and living applications. Rapid and reliable determination of H_2O_2 has been intensively pursued, for which a number of enzyme-based electrochemical biosensing platforms were built.[5] However, the use of enzyme proteins induces manufacturing complication, performance instability and expensiveness inherent to the core functional entity of biosensors.[30] Direct electrochemical route towards H_2O_2 sensing with enzyme-free earth-abundant materials therefore deserves attention. In this context, to further demonstrate the potential of the composite foam as a monolithic electrode for sensitive electroanalysis, the 3D-CuONA/Cu was fabricated into an enzyme-free electrode for H_2O_2 detection, whose properties were first evaluated by means of CV in phosphate buffer solution (PBS, pH 7.0), as shown in Fig. 4a. Clearly seen, when H_2O_2 was introduced, an obvious increase of cathodic current around -0.4 V can be identified, accompanied by slight decrease of oxidation current

in the reverse scan, typically indicating an electro-reduction process of H_2O_2. Fig. S5 shows the CV curves of 3D-CuONA/Cu foam at different scan rates and the corresponding calibration plot, which suggests the electrochemical process to be diffusion-controlled in nature. The possible mechanism for H_2O_2 sensing is illustrated in Fig. S6.[55,56]

Amperometry with successive analyte addition was performed to derive the linear relationship between the H_2O_2 concentration and the electrical signal feedback. The amperometric J-t curve shown in Fig. 4b exhibits a typical stair-like outline in correspondence with H_2O_2 injection, where the response time for 90% current change is less than 2 s and the current value generally reaches plateau within 2.5 s, as can be determined by the normalized ΔJ-Δt curves in Fig. 4c. An excellent sensitivity of 5.75 mA mM^{-1} cm^{-2} can be obtained from linear fitting (up to 700 uM) for the calibration plot in Fig. 4d. The limit of detection (LOD) reaches sub-micromolarity at 0.56 uM according to 3 signal-to-noise (S/N) ratio. The performance parameters of the 3D-CuONA/Cu are listed in Tab. S2 for comparison with some other H_2O_2 sensing electrodes reported in the literatures.

The stability of the sensor was confirmed by measuring the current responses to 10 uM H_2O_2 after 2-week storage at ambient condition without additional protection, which showed sensitivity retention over 90%. Amperometric responses to the target analyte and possible interference sources including uric acid (UA), ascorbic acid (AA) and glucose (Glu) were further examined (Fig. S7). As was found, introduction of UA, AA and

glucose generated limited amperometric feedbacks and addition of equimolar H_2O_2 resulted in significant leaping of the current curve, clearly proving its eligible selectivity. Next, we moved on to probe the ability of the sensor for practical analysis by applying the sensor to test commercial milk as primitively received and as spiked with H_2O_2 content, with the results given in Fig. S8. Upon addition of primitive milk samples, there was only a very small perturbation of current level, while for the milk sample spiked with H_2O_2, leaping of current is obvious, and the current response is the almost same as that of the standard H_2O_2 solution with the same concentration, suggesting its good anti-interference against the large amount of proteins, vitamins and carbohydrates in real milk.

Experimental

Preparation of 3D-CuONA/Cu composite foam

The preparation procedure started with formation of $Cu(OH)_2$ nanowire precursor on Cu foams. Briefly, after being cleaned with acetone and deionized water, a piece of Cu foam was immersed into a bath of etchant solution containing 0.12 M $(NH_4)_2S_2O_8$ and KOH about 25-fold (molar) of the persulfate oxidant for about 20 min. The as-treated Cu foam was marked by loss of metallic luster, accompanied by color change to light blue. Rinsed sufficiently with deionized water and ethanol, the sample dried under N_2 flow subsequently was heated in a furnace and went through thermolysis at 190 °C in air ambient for 3 h to obtain the final product, whose color is dull dark-brown.

Characterization

X-ray diffraction (XRD) was collected on a Rigaku D/MAX 2550 diffractometer equipped with a Cu Kα radiation generator. The morphological information was obtained using field-emission scanning electron microscopy (FE-SEM, Hitachi S4800) at an accelerating voltage of 15 kV. Detached CuO nanowires were photographed by transmission electron microscopy (JEOL, JEM 2011).

Electrochemical measurements

Cyclic voltammetry (CV) and electrochemical impedance spectroscopy (EIS) were performed with an electrochemical workstation (Autolab, PGSTAT302N). Under the three-electrode configuration, Pt electrode and Ag/AgCl electrode (KCl-saturated) were employed as the counter and reference electrodes, respectively. The working electrodes were 3D-CuONA/Cu or TO-CuO/Cu. EIS examination was conducted in a frequency range of 0.01-10k Hz at open-circuit potentials with an amplitude voltage of 10 mV. The electrolytes were 1 M NaOH and 0.1 M phosphate buffer solution (PBS, pH 7.0) for supercapacitance and H_2O_2 detection measurements, respectively. Before electrochemical measurements for detection application, the electrolyte was purged with nitrogen for 15 min to remove dissolved oxygen.

Conclusions

Highly facile and scalable preparation of monolithic 3D-CuONA/Cu composite was presented in this work, which combined efforts of room-temperature wet-chemical etching and hydroxide thermolysis at relatively low temperature. The 3D-CuONA/Cu composite achieved a high areal specific capacitance of 608 mF cm^{-2} at 2 mV s^{-1} and good capacitance retention of 88.6% after 4000 cycles, as well as an excellent sensitivity of 5.75 mA mM^{-1} cm^{-2}, bringing a favorable LOD as low as 0.56 uM for enzyme-free H_2O_2 detection. This top-down etching protocol opens possibility for low-cost and large-scale production of 3D composite foam to provide high-performance electrodes for functional electrochemical devices.

Acknowledgements

Notes and references

Key Laboratory for Ultrafine Materials of Ministry of Education, School of Materials Science and Engineering, East China University of Science and Technology, Shanghai 200237, China. Fax: +86 21 6425 0624; Tel: +86 21 6425 2022; E-mail: yhzhu@ecust.edu.cn (Y. Zhu); czli@ecust.edu.cn (C. Li).

† Electronic Supplementary Information (ESI) available: Additional texts, figures and tables as mentioned in the main text. See DOI: 10.1039/b000000x/

1   F. Cheng, J. Liang, Z. Tao and J. Chen, *Adv. Mater*, 2011, **23**, 1695-1715.

2   M. Winter and R. J. Brodd, *Chem. Rev.*, 2004, **104**, 4245-4270.

3   M. G. Walter, E. L. Warren, J. R. McKone, S. W. Boettcher, Q. Mi, E. A. Santori and N. S. Lewis, *Chem. Rev.*, 2010, **110**, 6446–6473.

4   E. Brillas, I. Sirés and M. A. Oturan, *Chem. Rev.*, 2009, **109**, 6570-6631.

5   D. W. Kimmel, G. LeBlanc, M. E. Meschievitz and D. E. Cliffel, *Anal. Chem.*, 2011, **84**, 685-707.

6   J. Zhu, J. Jiang, Z. Sun, J. Luo, Z. Fan, X. Huang, H. Zhang and T. Yu, *Small*, 2014, **10**, 2937–2945.

7   B. Fang, C. Zhang, W. Zhang and G. Wang, *Electrochim. Acta*, 2009, **55**, 178-182.

8   G. Wang, X. Lu, T. Zhai, Y. Ling, H. Wang, Y. Tong and Y. Li, *Nanoscale*, 2012, **4**, 3123-3127.

9   M. Kawamori, T. Asai, Y. Shirai, S. Yagi, M. Oishi, T. Ichitsubo and E. Matsubara, *Nano Lett.*, 2014, **14**, 1932-1937.

10 J. Yan, Z. Fan, W. Sun, G. Ning, T. Wei, Q. Zhang, R. Zhang, L. Zhi and F. Wei, *Adv. Funct. Mater.*, 2012, **22**, 2632-2641.

11 X. Xia, J. Tu, Y. Zhang, J. Chen, X. Wang, C. Gu, C. Guan, J. Luo and H. J. Fan, *Chem. Mater.*, 2012, **24**, 3793-3799.

12 H. Chen, Q. Zhang, J. Wang, D. Xu, X. Li, Y. Yang and K. Zhang, *J. Mater. Chem. A*, 2014, **2**, 8483-8490.

13 J. Wang, Q. Zhang, X. Lia, D. Xu, Z. Wang, H. Guo and K. Zhang, *Nano Energy*, 2014, **6**, 19-26.

14 X. Ke, Y. Xu, C. Yu, J. Zhao, G. Cui, D. Higgins, Z. Chen, Q. Li, H. Xu and G. Wu, *J. Mater. Chem*. A, 2014, **2**, 16474-16479.

15 Y. Fan, R. Liu, W. Du, Q. Lu, H. Pang and F. Gao, *J. Mater. Chem.*, 2012, **22**, 12609-12617.

16 K. Khun, Z. H. Ibupoto and M. Willander, *Electroanalysis*, 2013, **25**, 1425-1432.

17 S. B. Wang, C. H. Hsiao, S. J. Chang, K. T. Lam, K. H. Wen, S. C. Hung, S. J. Young and B. R. Huang. *Sens. Actuators*, *A*, 2011, **171**, 207-211.

18 S. Yuan, X. Huang, D. Ma, H. Wang, F. Meng and X. Zhang, *Adv. Mater.*, 2014, **26**, 2273-2279.

19 A. Kargar, Y. Jing, S. J. Kim, C. T. Riley, X. Pan and D. Wang, *ACS Nano*, 2013, **7**, 11112-11120.

20 M. Zhi, C. Xiang, J. Li, M. Li and N. Wu, *Nanoscale*, 2013, **5**, 72-88.

21 X. Zhang, W. Shi, J. Zhu, D. J. Kharistal, W. Zhao, B. S. Lalia, H. H. Hng and Q. Yan, *ACS Nano*, 2011, **5**, 2013-2019.

22 Y. X. Zhang, M. Huang, M. Kuang, C. P. Liu, J. L. Tan, M. Dong, Y. Yuan, X. L. Zhao and Z. Wen, *Int. J. Electrochem. Sci.*, 2013, **8**, 1366-1381.

23 Y. X. Zhang, M. Huang, F. Li and Z. Q. Wen, *Int. J. Electrochem. Sci.*, 2013, **8**, 8645-8661.

24 C. Dong, Y. Wang, J. Xu, G. Cheng, W. Yang, T. Kou, Z. Zhang and Y. Ding, *J. Mater. Chem. A*, 2014, **2**, 18229–18235.

25 S. K. Shinde, D. P. Dubal, G. S. Ghodake, D. Y. Kim and V. J. Fulari, *J. Electroanal. Chem.*, 2014, **732**, 80-85.

26 M. J. Deng, C. C. Wang, P. J. Ho, C. M. Lin, J. M. Chen and K. T. Lu, *J. Mater. Chem. A*, 2014, **2**, 12857-12865.

27 G. Wang, J. Huang, S. Chen, Y. Gao and D. Cao, *J. Power Sources*, 2011, **196**, 5756-5760.

28 D. P. Dubal, D. S. Dhawale, R. R. Salunkhe, V. S. Jamdade and C. D. Lokhande, *J. Alloys Compd.*, 2010, **492**, 26-30.

29 W. Jia, M. Guo, Z. Zheng, T. Yu, Y. Wang, E. G. Rodriguez and Y. Lei, *Electroanalysis*, 2008, **20**, 2153-2157.

30 C. Kong, L. Tang, X. Zhang, S. Sun, S. Yang, X. Song and Z. Yang, *J. Mater. Chem. A*, 2014, **2**, 7306–7312.

31 Z. Guo, M. L. Seol, M. S. Kim, J. H. Ahn, Y. K. Choi, J. H. Liu and X. J. Huang, *Nanoscale*, 2012, **4**, 7525-7531.

32 S. Reddy, B. E. K. Swamy and H. Jayadevappa, *Electrochim. Acta*, 2012, **61**, 78-86.

33 S. Saadat, J. Zhu, D. H. Sim, H. H. Hng, R. Yazami and Q. Yan, *J. Mater. Chem. A*, 2013, **1**, 8672-8678.

34 C. Zhu, D. Chao, J. Sun, I. M. Bacho, Z. Fan, C. F. Ng, X. Xia, H. Huang, H. Zhang, Z. X. Shen, G. Ding, and H. J. Fan, *Adv. Mater. Interfaces*, DOI: 10.1002/admi.201400499.

35   X. Jiang , X. Yang , Y. Zhu, H. Jiang , Y. Yao , P. Zhao and C. Li, *J. Mater. Chem. A*, 2014, **2**, 11124-11133.

36 Y. K. Hsu, C. H. Yu, H. H. Lin, Y. C. Chen and YG Lin, *J. Electroanal. Chem.*, 2013, **704**, 19-23.

37 A. Kargar, S. S. Partokia, M. T. Niu, P. Allameh, M. Yang, S. May, J. S. Cheung, K. Sun, K. Xu and D. Wang, *Nanotechnology*, 2014, **25**, 205401.

38 W. Zhang, X. Wen and S. Yang, *Inorg. Chem.*, 2003, **42**, 5005-5014.

39 J. Huang, Y. Zhu, X. Yang, W. Chen, Y. Zhou, C. Li, *Nanoscale*, 2015, **7**, 559-569.

40 J. Rodríguez-Moreno, E. Navarrete-Astorga, E. A. Dalchiele, R. Schrebler, J. R. Ramos-Barradoa and F. Martina, *Chem. Commun.*, 2014, **50**, 5652-5655.

41 V. D. Patake, S. S. Joshi, C. D. Lokhande and O. S. Joo, *Mater. Chem. Phys.*, 2009, **114**, 6-9.

42 K. V. Gurav, U. M. Patil, S. W. Shin, G. L. Agawane, M. P. Suryawanshi, S. M. Pawar, P. S. Patil, C. D. Lokhande and J. H. Kim, *J. Alloys Compd.*, 2013, **573**, 27-31.

43 Y. K. Hsu, Y. C. Chen and Y. G. Lin, *Electrochim. Acta*, 2014, **139**, 401-407.

44 Y. K. Hsu, Y. C. Chen and Y. G. Lin, *J. Electroanal. Chem.*, 2012, **673**, 43-47.

45 Z. Endut, M. Hamdi and W. J. Basirun, *Thin Solid Films*, 2013, **528**, 213-216.

46 Y. X. Zhang, F. Li and M. Huang. *Mater. Lett.*, 2013, **112**, 203-206.

47 R. Li, X. Ren, F. Zhang, C. Du and J. Liu, *Chem. Commun.*, 2012, **48**, 5010-5012.

48 J. H. Kim, S. H. Kang, K. Zhu, J. Y. Kim, N. R. Neale and A. J. Frank, *Chem. Commun.*, 2011, **47**, 5214-5216.

49 J. B. Wu, Y. Lin, X. H. Xia, J. Y. Xu and Q. Y. Shi, *Electrochim. Acta*, 2011, **56**, 7163-7170.

50 G. Zhang, W. Li, K. Xie, F. Yu and H. Huang, *Adv. Funct. Mater.*, 2013, **23**, 3675-3681.

51 B. Vidhyadharan, I. I. Misnon, R. A. Aziz, K. P. Padmasree, M. M. Yusoffa and R. Jose, *J. Mater. Chem. A*, 2014, **2**, 6578-6588.

52 A. Pendashteh, M. F. Mousavi and M. S. Rahmanifar, *Electrochim. Acta*, 2013, **88**, 347-357.

53 Y. Liu, H. Huang and X. Peng, *Electrochim. Acta*, 2013, **104**, 289-294.

54 D. P. Dubal, G. S. Gund, C. D. Lokhande and R. Holze, *Mater. Res. Bull.*, 2013, **48**, 923-928.

55 J. Huang, Y. Zhu, H. Zhong, X. Yang and C. Li, *ACS Appl. Mater. Interfaces*, 2014, **6**, 7055-7062.

56 F. Xu, M. Deng, G. Li, S. Chen and L. Wang, *Electrochim. Acta*, 2013, **88**, 59-65.

Graphical Abstract
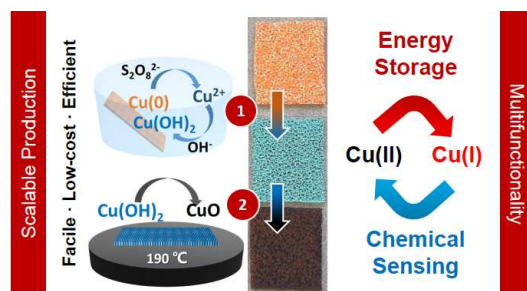
Facile nanoengineering of commercial copper foam was used to prepare 3D free-standing CuO nanowire for enhanced electrochemical applications including pseudo-capacitance energy storage and electroanalysis of hydrogen peroxide.